Metals & corrosion

Relief of strain hardening in deformed Inconel 718 by high-density pulsed electric current

Shaojie Gu[1], Yi Cui[1], Yasuhiro Kimura[1], Yuhki Toku[1], and Yang Ju[1,*]

[1] *Department of Micro-Nano Mechanical Science and Engineering, Graduate School of Engineering, Nagoya University, Nagoya, Japan*

ABSTRACT

The effect of high-density pulsed electric current (HDPEC) on the microstructure evolution and corresponding changes in the mechanical properties of the deformed Ni-based alloy Inconel 718 was investigated. After HDPEC treatment, the strain hardening was fully relieved and the ductility recovered correspondingly. The results show that the dislocation density plays a dominant role, and the grain size has a side effect on the strain-hardening relief. Furthermore, the correlation between the mechanical properties and microstructure evolution affected by HDPEC was clarified. HDPEC treatment provides a way to alter the microstructure and thus tailor the mechanical properties of the deformed components. Hence, it is applicable to the metal-forming field to achieve rapid relief of strain hardening and enhance formability.

GRAPHICAL ABSTRACT
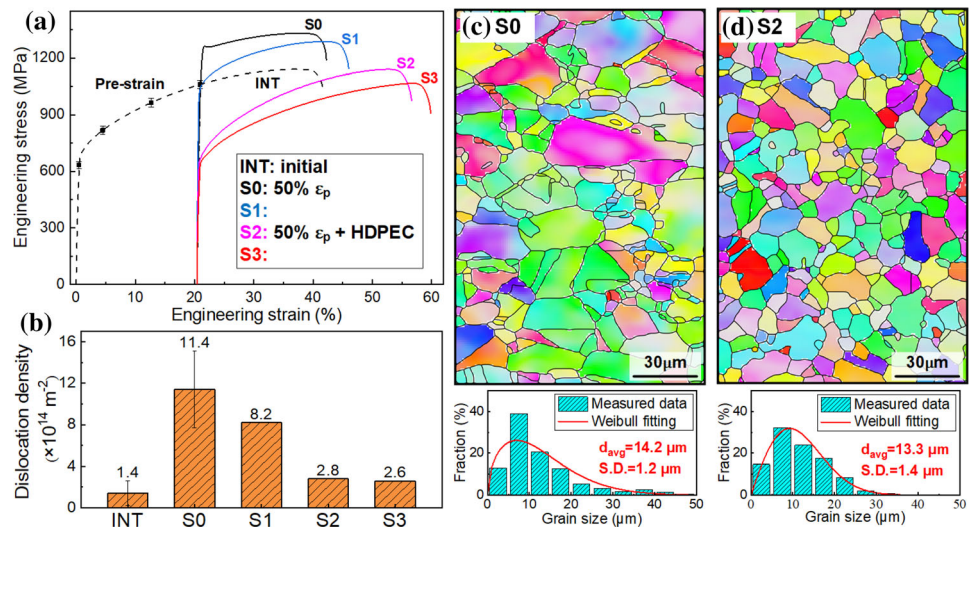
Introduction

Strain hardening is undesirable in metal forming because the cold-worked pieces possess high strength but weak ductility, resulting in poor forming quality and an additional requirement of forming force. Consequently, intermediate annealing is needed to restore the ductility loss during repeated cold working in the processing of pieces [1]. However, it requires a high temperature to heat the deformed components for a long time, which is time-consuming and laborious. The improvement of ductility during annealing is mainly due to the recrystallization and dislocation annihilation, which is low-efficiency [2, 3]. Recently, the treatment of high-density electric current as a low-cost and highly efficient method has been introduced to relieve the plastic strain and residual stress [4, 5]. Moreover, several reports have delineated that the relief of strain hardening is attributed to the rapid recrystallization of the deformed grains under the treatment of electric current, and the rapid recrystallization was promoted by the coupling thermal (Joule heating) and athermal (electron wind force) effects [5–10]. However, so far, it has been concluded that the strain-hardening relief resulted from recrystallization, but the contribution of dislocation annihilation has not yet been investigated.

Therefore, in this study, the evolution of both grain refinement and dislocation annihilation induced by high-density electric current was investigated in detail, and their contributions to strain-hardening relief were clarified based on the quantitative analysis. The effect of high-density pulsed electric current (HDPEC) under different conditions on the relief of strain hardening of deformed Inconel 718 was investigated systematically. The quantitative analysis of the corresponding microstructure evolution was conducted using X-ray diffraction (XRD) and electron backscatter diffraction (EBSD). The correlation between the mechanical properties and microstructure evolution was established, and it was found that dislocation annihilation is the crucial factor resulting in the relief of strain hardening, while grain size evolution acted as a side effect.

Experimental procedures

The material used was a Ni-based alloy Inconel 718 (IN718); the chemical composition is listed in Table 1. The sample was dumbbell-shaped, with a gauge length of 22 mm and a cross-section area of 3.5 × 1.6

Table 1 Chemical composition (wt.%) of IN718

Ni	C	Mn	Fe	Cu	Cr	Al	Ti	Co	Mo	Nb	P	S
Bal.	0.03	0.10	17.67	0.12	18.59	0.55	0.93	0.19	2.88	5.07	0.009	0.001

mm^2 at the tension part. It was formed by wire cutting. The surface of the sample was ground using emery papers and then polished to a mirror surface with a 3 μm water-based diamond suspension on a polishing machine (LaboPol-20, STRUERS). For EBSD observation, a colloidal silica suspension solution (OP-S suspension, STREURS) was used to remove the deformed layers during polishing.

The tensile test was conducted on a hydraulic-driven testing machine (SHIMAZU) at room temperature (25 °C) with a loading speed of 0.03 mm/s. Initially, the tensile stretch was used to introduce a pre-strain of 20.5% (approximately 50% of the plastic strain at the breaking point, denoted by 50% ε_p) into the samples. The current treatment was then performed on the pre-strained samples. The samples are listed in Table 2. The sample INT represents the initial case without pre-strain and HDPEC treatment, and sample S0 is the pre-strained sample without current treatment. Samples S1–S3 were first pre-strained and then HDPEC treated under a current density of 300 A/mm^2 with pulse duration times of 13.33, 16.67, and 20 ms for 3 pulses. The interval time of each pulse was 1 s. Thus, the total treatment time for each sample was 40, 50, and 60 ms, respectively.

X-ray diffraction (XRD) was employed to measure the residual stress in the samples. Measurements were carried out on a Rigaku X-ray stress analyzer using Cu-Kα radiation. The 2θ-$sin^2\psi$ method was used to calculate the surface residual stress [11, 12], and the average of the negative and positive tilt angles at $\psi = 0°$, $\pm 14.48°$, $\pm 20.7°$, $\pm 25.66°$, $\pm 30°$ on the (220) peak was used to determine the relationship between 2θ and $sin^2\psi$. The XRD line profile

analysis method was used to calculate the dislocation density using the modified Williamson–Hall and Warren–Averbach methods [13–15]. Crystal orientations were measured using an EBSD detector (NordlysNano, Oxford Instruments) interfaced with a scanning electron microscope (SEM, HITACHI). Data processing was performed using commercial software (MATLAB, MathWorks) along with an open-source toolbox, MTEX [16]. The surface morphology and fractography were observed using SEM (JSM-7200F, JEOL).

Results

Mechanical properties and residual stress

The engineering stress–strain curves of all samples (listed in Table 2) are plotted in Fig. 1a, and the mechanical properties (yield stress and elongation) of each sample are shown in Fig. 1b. The initial sample INT shows a regular yield stress of $\sigma_y = 623$ MPa and a good elongation of $\varepsilon_f = 41.3\%$. After pre-straining, sample S0 presents a heavy strain hardening with a high yield strength of $\sigma_y = 1235$ MPa and a decreased elongation of $\varepsilon_f = 21.3\%$. For the HDPEC-treated samples S1–S3, the strength was restored and the elongation increased gradually with an increase in the treatment time of the pulsed current. Among them, the strain hardening of sample S2 was almost completely relieved with a relatively high elongation compared to the initial one. Moreover, sample S3 shows lower strength than the initial sample with the highest elongation.

Table 2 Samples and treatment conditions

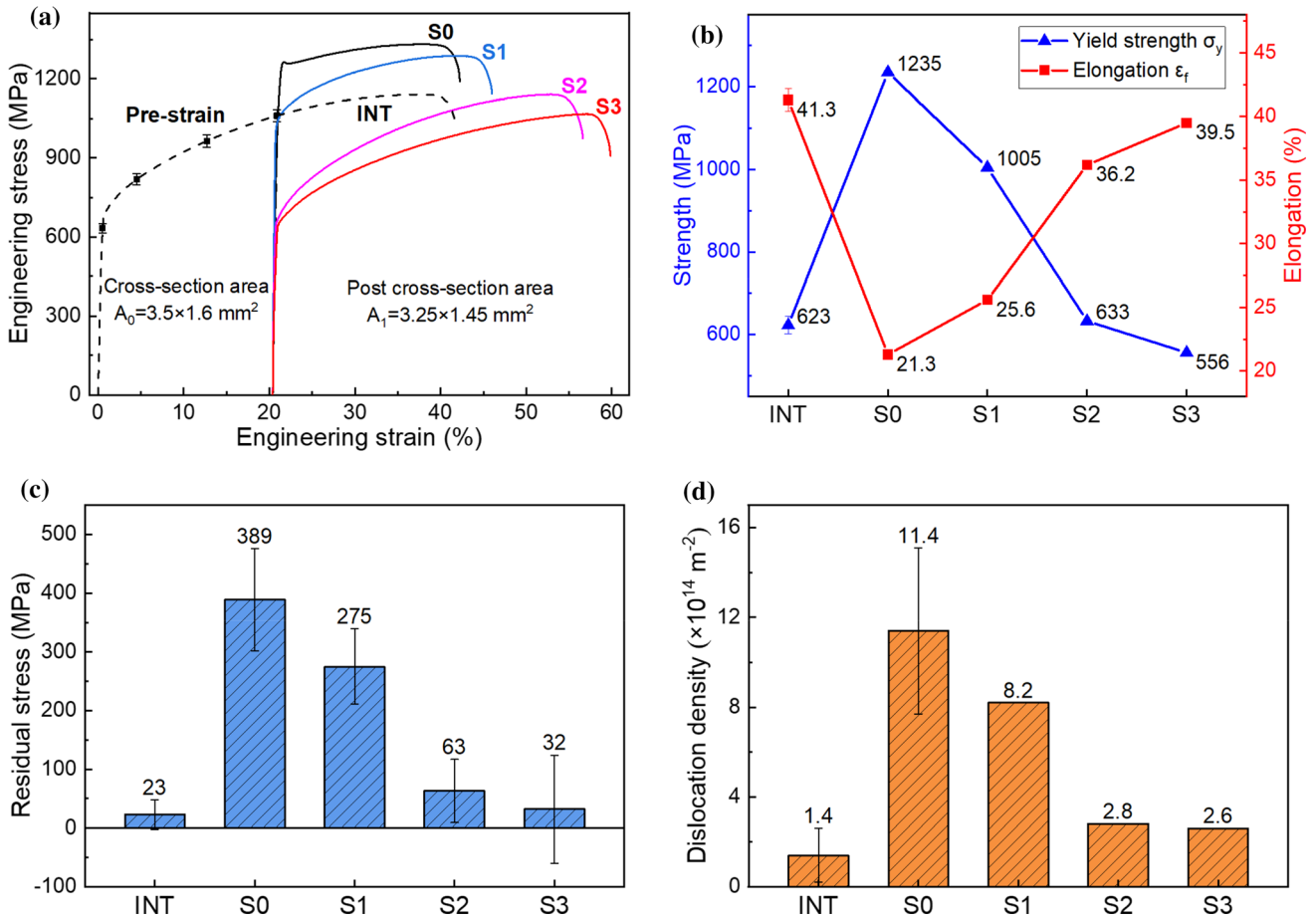| Sample	Pre-strain	HDPEC treatment			
		Current density (A/mm^2)	Duration time of pulse (ms)	Interval time of pulse (s)	Number of pulse
INT	–	–	–	–	–
S0	50% ε_p	–	–	–	–
S1	50% ε_p	300	13.33	1	3
S2	50% ε_p	300	16.67	1	3
S3	50% ε_p	300	20	1	3

Figure 1 Changes of mechanical properties and residual stress in each sample. **a** engineering stress–strain curves, **b** plots of yield stress and elongation, **c** residual stress, and **d** dislocation density..

The residual stress and dislocation density of each sample were estimated by XRD, and the results are shown in Fig. 1c, d. After pre-straining, the residual stress of sample S0 increased from 23 to 389 MPa, and the dislocation density increased from 1.4×10^{14} to 11.4×10^{14} m^{-2}. After the HDPEC treatments, the residual stress was gradually relieved, and the dislocation density decreased in the same manner. In samples S2 and S3, the residual stress was almost completely relieved with a decrease in dislocation density.

Grain morphology and local deformation

The EBSD orientation maps of each sample are shown in Fig. 2, where the grain size distributions with Weibull fitting [17] are also provided. The uniform grain morphology of the initial sample INT was obtained with a mean grain size of 14.5 μm, as shown in Fig. 2a. The elongated morphology and dispersed

color in grains were observed in sample S0 with a slight change in grain size (14.2 μm), as shown in Fig. 2b. After HDPEC treatment, the deformation in the grains of sample S1 remained unchanged, while some small grains were formed, as shown in Fig. 2c, resulting in a decrease in the mean grain size to 11.5 μm. When the HDPEC treatment time was increased to 50 ms (sample S2), refined grains were formed with a mean grain size of 13.3 μm, as shown in Fig. 2d. After increasing the treatment time further (sample S3), the mean grain size increased to 15.5 μm, as shown in Fig. 2e.

Local misorientation, also known as kernel average misorientation (KAM), is commonly used to indicate grain-scale plastic deformation [18, 19]. The KAM maps of each sample corresponding to the EBSD orientation maps are shown in Fig. 3, and the misorientation distributions of each case are also presented. Sample INT shows a uniform blue color (low KAM value) with a mean value of 0.05°, while
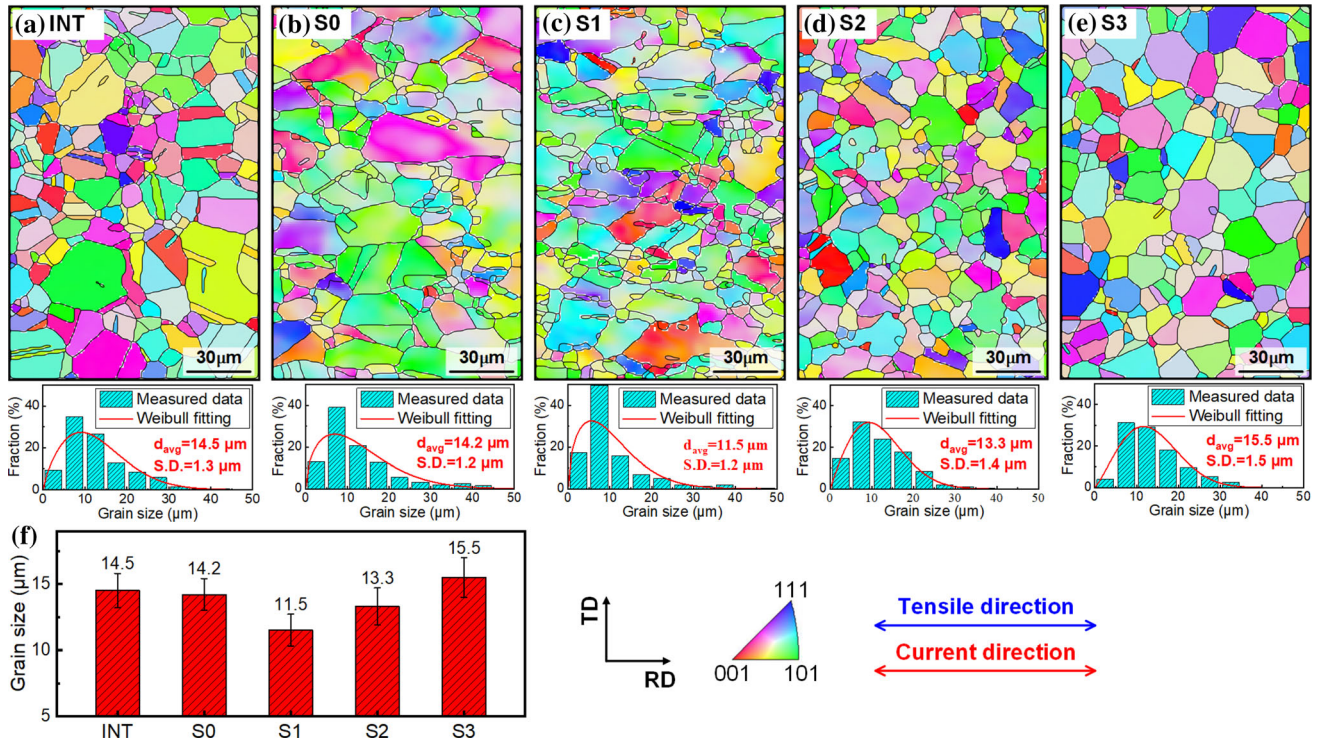
Figure 2 EBSD orientation maps and grain size distributions of **a** INT, **b** S0, **c** S1, **d** S2, **e** S3, and **f** mean grain size of each sample. The EBSD map covers a range of 120×180 μm^2 with a step size of 1 μm. RD and TD represent the rolling direction and transverse direction, respectively. The tensile and current directions are horizontal.
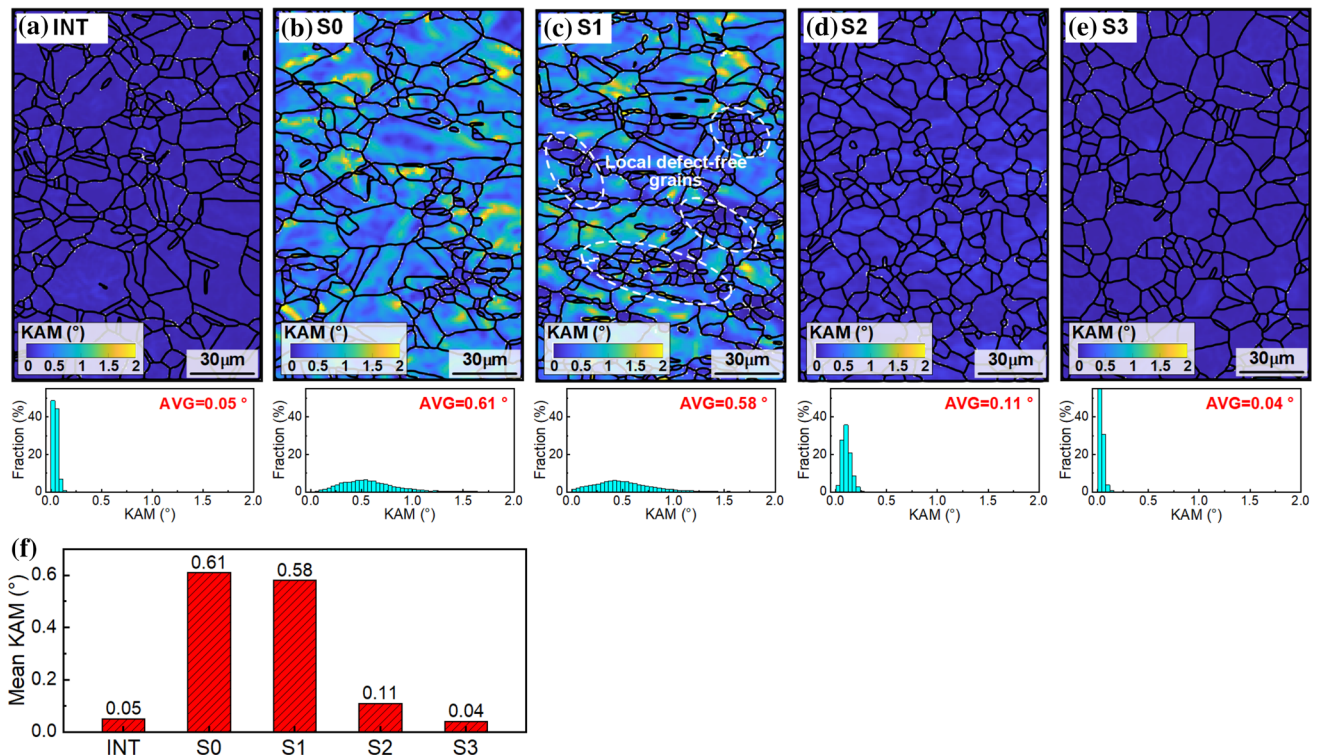

Figure 3 KAM maps and corresponding misorientation distributions of **a** INT, **b** S0, **c** S1, **d** S2, **e** S3, and **f** mean KAM value of each sample.

sample S0 illustrates inhomogeneous colors in the KAM map with a mean KAM value of 0.61° due to the pre-strain, as shown in Fig. 3a, b. After HDPEC treatment, sample S1 almost retained the inhomogeneous colors in the KAM map, in which some small blue grains appeared, leading to a decrease in the mean KAM value to 0.58°, as shown in Fig. 3c. After HDPEC treatment time was increased to 50 ms and 60 ms (samples S2 and S3), uniform grains with a low KAM value were observed, as shown in Fig. 3d, e, indicating that the deformation in grains was recovered completely.

Surface morphology and fractography

Figure 4 shows the SEM backscattered electron (BSE) images of each sample to investigate the surface morphology evolution. The initial sample INT shows a uniform grain morphology filled with needle-shaped δ-phase, NbC particles, and tiny TiN particles, which was identified by energy-dispersive X-ray spectroscopy (EDS), as shown in Fig. 4a. The slip bands were observed in the deformed sample S0, as shown in Fig. 4b, and the intergranular microvoids, debonding, and broken carbides were nucleated owing to uncoordinated deformation between the particles and grains. After applying the minor HDPEC, the remaining slip bands were observed in sample S1, as shown in Fig. 4c. After increasing HDPEC treatment time (samples S2 and S3), the

uniform grains were obtained, as shown in Fig. 4d, e. Meanwhile, the slip bands, microvoids, and debonding were well healed, while the breaks in the carbides remained.

The fracture characteristics of each sample are presented in Fig. 5. The mean dimple diameters estimated using the open-source program ImageJ are also presented. The fracture morphology of sample S0 depicts a ductile fracture with a mean dimple diameter of 4.2 μm, as shown in Fig. 5a. Inhomogeneous dimples were observed in sample S1 with some small dimples, and the average dimple diameter was slightly decreased (4.0 μm). Sample S2 presents homogeneous dimples with a uniform size of 6.1 μm, indicating better ductility than sample S0 (Fig. 5c). After increasing the treatment time to 60 ms (sample S3), larger dimples were obtained with a mean value of 7.4 μm.

Discussion

Strain-hardening relief and ductility recovery

There are four common strategies for strengthening materials: strain hardening (dislocation strengthening) [20], solid solution strengthening [21], precipitation strengthening [22], and fine-grained strengthening [23, 24]. In the results shown above, the
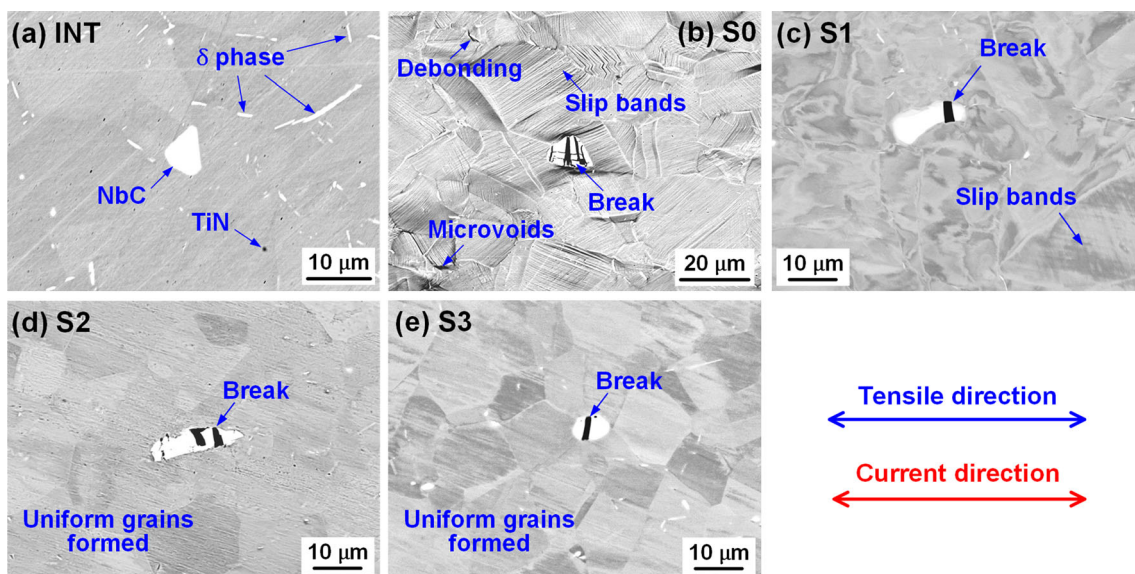

Figure 4 BSE images of **a** INT, **b** S0, **c** S1, **d** S2, and **e** S3. The bright particles are NbC carbide, the needle-shaped white phases the δ-phase (Ni₃Nb), and the tiny dark spots the TiN particle. The directions of tensile and current are horizontal.
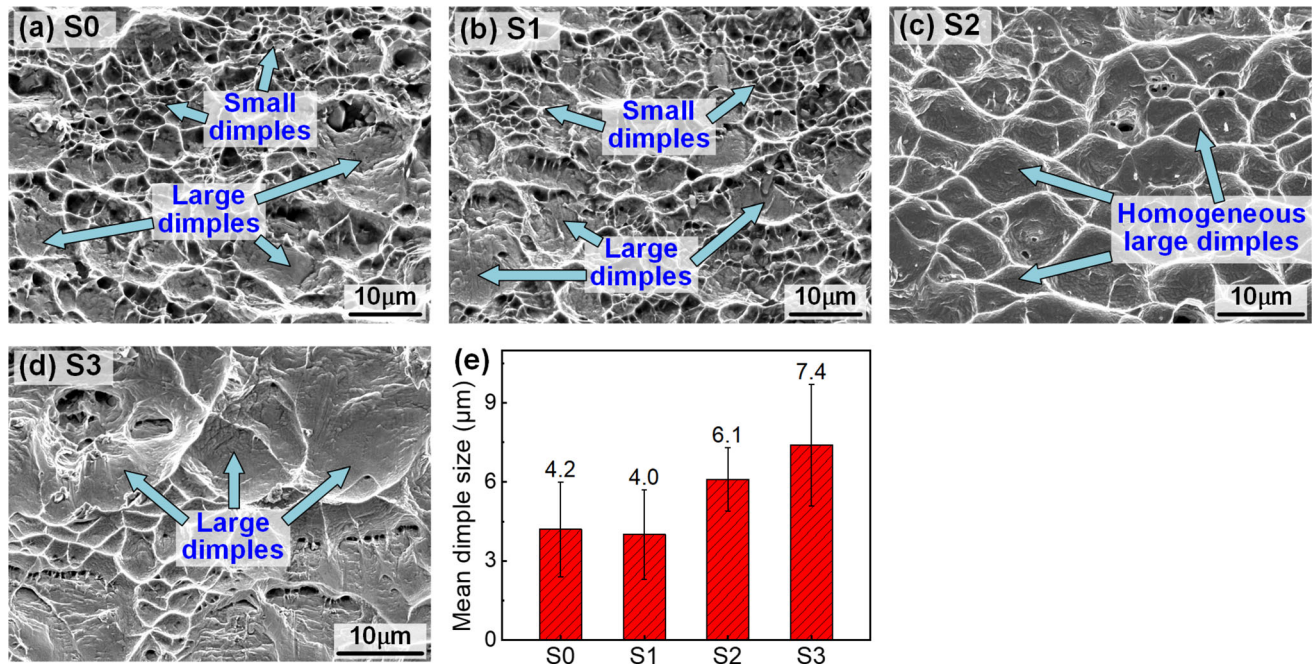
Figure 5 SEM fractography of **a** S0, **b** S1, **c** S2, **d** S3, and **e** mean dimple diameter of each sample.

strength reduction induced by HDPEC was mainly attributed to the change in dislocation density and grain size, which can be described by

$$\Delta\sigma = \Delta\sigma_d + \Delta\sigma_g \qquad (1)$$

where $\Delta\sigma$ represents the change in the strength. The parameters $\Delta\sigma_d$ and $\Delta\sigma_g$ are the strength changes due to the dislocation density and grain size, respectively.

The contribution of dislocation, $\Delta\sigma_d$, can be estimated using the Taylor hardening law [25, 26] as

$$\Delta\sigma_d = \alpha MGb\left(\rho_2^{1/2} - \rho_1^{1/2}\right) \qquad (2)$$

where α was determined to be 0.63, by linearly fitting the relationship between the strength and the square root of the dislocation density at different pre-strains obtained in preliminary experiments. Parameter M is the Taylor factor, taken as 3.1 for FCC metals [2], G is the shear modulus, taken as 74 GPa (IN718), and b is the Burgers vector, taken as 0.255 nm (b(FCC) $= \frac{a}{2}$ <110>). Parameters ρ_1 and ρ_2 are the dislocation densities before and after HDPEC treatment, respectively. For sample S2, the dislocation density before and after HDPEC treatment is 1.14×10^{15} m^{-2} and 0.28×10^{15} m^{-2}, respectively, as shown in Fig. 1d. By substituting the dislocation density in Eq. (2), the reduction in $\Delta\sigma_d$ was found to be -627.6 MPa.

The contribution of $\Delta\sigma_g$ can be evaluated using the Hall–Petch relationship [24] as

$$\Delta\sigma_g = k\left(d_2^{-1/2} - d_1^{-1/2}\right) \qquad (3)$$

where parameters d_1 and d_2 are the average grain sizes before and after HDPEC treatment, respectively. Parameter k is a constant, which can take 1175.93 MPa·µm$^{1/2}$ for IN718 [27]. For sample S2, the grain sizes before and after the HDPEC treatment are 14.2 µm and 13.3 µm, respectively, as shown in Fig. 2f. Thus, the contribution of $\Delta\sigma_g$ is 10.4 MPa.

Therefore, the total strength reduction calculated from the above equations is -617.2 MPa, which is in good agreement with the experimental results of -602 MPa, that is, from 1235 to 633 MPa, as shown in Fig. 1b. As shown in Fig. 2, the grain size of sample S2 did not change significantly after HDPEC treatment. Thus, dislocation density is the dominant reason for strain-hardening relief, while grain size only has a side effect.

Micro-defects such as dislocations, interstitial atoms, and grain boundaries can cause local distortion and strain of the lattice and generate micro- or further macro-residual stress [28, 29]. Hence, the high residual stress of sample S0 was mainly owing to the high dislocation density associated with the pre-strain. However, after the HDPEC treatment, the residual stress was partially or fully relieved owing

to the decreased dislocation density, as shown in Fig. 1c, d.

However, the ductility is impaired by strain hardening because the existing dislocations hinder the multiplication and motion of new dislocations [30]. Hence, the removal of dislocations by the HDPEC treatment, as shown in Fig. 1d, restored the deformability and thus resulted in the recovery of ductility of the HDPEC-treated samples.

Dislocation removal and grain refinement

The driven electron collides with the atom and can exert a force, electron wind force (EWF), on the atom by momentum transfer [31]. Moreover, the EWF can also drive the dislocation to glide and enhance dislocation annihilation [32]. Xiang et al. [33] found that the dislocation structure was rearranged parallel to the direction of the current flow, which directly demonstrates the driving effect of the EWF. Therefore, with the help of the driving effect of EWF induced by HDPEC, dislocation annihilation can be accelerated by increasing the combination of dipole dislocations [34] and promoting dislocation gliding to the grain boundary [35]. As shown in Fig. 1d, the dislocation density gradually decreases after HDPEC treatment. In addition, as shown in Fig. 3, the KAM maps show the same trend, in which the value was progressively reduced by increasing the treatment time of HDPEC. Since KAM is used to estimate the geometrically necessary dislocations [36], the decrease in KAM values after the HDPEC treatment also indicates a decrease in dislocations in grains by EWF.

Furthermore, the EWF tends to enhance the dislocation motion and entanglement, thereby resulting in the formation of local defect-free grains near the grain boundary. As shown in Fig. 3c, some small grains with a low KAM value were created in sample S1 after HDPEC treatment. When the HDPEC treatment reached sufficient energy with a long treatment time, all the movable dislocations moved to the grain boundaries, resulting in the formation of defect-free grains or absorption by grain boundaries. Consequently, complete grain refinement was realized in sample S2, and large uniform grains in sample S3 were obtained. Grain refinement is considered to have an important effect on the ductility recovery.

Micro-defects healing and fractographic evolution

As shown in Fig. 4, after HDPEC treatment, the slip bands, microvoids, and debonding were well healed. Slip band repair is possible due to dislocation annihilation, and the healing of microvoids and debonding could be due to the impact of high-density electrons on the defects. Song et al. [37, 38] and Yang et al. [39] also reported that the pre-strain-induced voids or cracks were healed entirely after the treatment of electric current, and the damage-healing effect was the result of local heating and local compressive stress around the defects. However, the break in NbC particles was not healed by HDPEC treatment, as shown in Fig. 4c–e, which is considered to be due to the relatively large dimensions of the particles and the brittle property of NbC.

It is well known that the appearance of dimples is related to voids [40, 41]. Owing to the inconsecutive properties of the grain boundary, it is a vital resource to initiate voids during deformation. With continued deformation, the voids tend to propagate and merge and finally cause the fracture. Qin et al. [23] reported that the dimple is associated with the grain boundary, where the mean diameter of the dimple is positively related to the square root of the grain size. Hence, the inhomogeneous small dimples in sample S1, as shown in Fig. 5b, can be attributed to the local refinement of the small grains. The complete grain refinement of sample S2 induced by HDPEC treatment resulted in homogeneous and large dimples, as shown in Fig. 5c, indicating that the ductility was enhanced compared with sample S0. The large dimples in sample S3 were related to the large uniformed grains in the sample (Fig. 5d).

Conclusions

The effect of HDPEC on the relief of strain hardening and ductility recovery of the deformed IN718 alloy was studied. Furthermore, the correlation between the mechanical properties and microstructure evolution of HDPEC treatment was investigated in detail. The main conclusions are as follows:

1. Strain hardening was fully relieved by HDPEC treatment. In addition, the results show that the dislocation density plays a dominant role in

strain-hardening relief, while grain size acts as a side effect.

2. The dislocations were rapidly removed by HDPEC, which resulted in local deformation recovery and grain refinement, thereby leading to ductility recovery.

3. Homogeneous and large dimples were obtained in the HDPEC-treated sample, and the slip bands, microvoids, and debonding in the pre-strained sample healed after HDPEC treatment.

Therefore, owing to the fast and efficient features in dislocation removal, HDPEC treatment can alter the microstructure and tailor the mechanical properties of the deformed materials. Consequently, it can be applied to metal forming, achieving rapid relief of the strain hardening of the cold-worked pieces, thereby enhancing the forming efficiency.

Acknowledgements

Author contributions

Shaojie Gu contributed to the conceptualization, investigation, data curation, formal analysis, and writing of the original draft. Yi Cui helped in the validation, investigation, and writing—review and editing. Yasuhiro Kimura was involved in the data curation and writing—review and editing. Yuhki Toku helped in the validation and writing—review and editing. Yang Ju contributed to the conceptualization, methodology, supervision, project administration, resources, and writing—review and editing.

Declarations

Conflict of interest The authors declare no conflict of interest.

References

[1] Black JT, Kohser RA, DeGarmo EP (2012) DeGarmo's materials and processes in manufacturing, 11th edn. Wiley, Hoboken

[2] Hull D, Bacon DJ (2011) Introduction to dislocations, 5th edn. Elsevier/Butterworth-Heinemann, Amsterdam

[3] Rollett A, Humphreys FJ, Rohrer GS, Hatherly M (2004) Recrystallization and Related Annealing Phenomena, 2nd edn. Pergamon, Amsterdam, Boston

[4] Pan L, Wang B, Xu Z (2019) Effects of electropulsing treatment on residual stresses of high elastic cobalt-base alloy ISO 5832–7. J Alloy Compd 792:994–999. https://doi.org/10.1016/j.jallcom.2019.04.091

[5] Tang Y, Hosoi A, Morita Y, Ju Y (2013) Restoration of fatigue damage in stainless steel by high-density electric current. Int J Fatigue 56:69–74. https://doi.org/10.1016/j.ijfatigue.2013.08.012

[6] Jiang Y, Tang G, Shek C et al (2012) Mechanism of electropulsing induced recrystallization in a cold-rolled Mg–9Al–1Zn alloy. J Alloy Compd 536:94–105. https://doi.org/10.1016/j.jallcom.2012.05.014

[7] Jin W, Fan J, Zhang H et al (2015) Microstructure, mechanical properties and static recrystallization behavior of the rolled ZK60 magnesium alloy sheets processed by electropulsing treatment. J Alloy Compd 646:1–9. https://doi.org/10.1016/j.jallcom.2015.04.196

[8] Zhu R, Jiang Y, Guan L et al (2016) Difference in recrystallization between electropulsing-treated and furnace-treated NiTi alloy. J Alloy Compd 658:548–554. https://doi.org/10.1016/j.jallcom.2015.10.239

[9] Park J-W, Jeong H-J, Jin S-W et al (2017) Effect of electric current on recrystallization kinetics in interstitial free steel and AZ31 magnesium alloy. Mater Charact 133:70–76. https://doi.org/10.1016/j.matchar.2017.09.021

[10] Jeong H-J, Kim M-J, Choi S-J et al (2020) Microstructure reset-based self-healing method using sub-second electric pulsing for metallic materials. Appl Mater Today 20:100755. https://doi.org/10.1016/j.apmt.2020.100755

[11] Eigenmann B, Macherauch E (1996) Röntgenographische Untersuchung von Spannungszuständen in Werkstoffen. Teil III. Fortsetzung von Matwiss. und Werkstofftechn. Heft 3/1995, S. 148–160 und Heft 4/1995, S. 199–216. Mat-wiss u Werkstofftech 27:426–437. https://doi.org/10.1002/mawe.19960270907

[12] Eigenmann B, Macherauch E (1996) Röntgenographische Untersuchung von Spannungszuständen in Werkstoffen Teil IV. Fortsetzung von Matwiss. und Werkstofftechn. Heft 3/1995, S. 148–160, Heft 4/1995, S. 199–216 und Heft 9/1996, S. 426–437. Mat-wiss u Werkstofftech 27:491–501. https://doi.org/10.1002/mawe.19960271010

[13] Ungár T, Ott S, Sanders PG et al (1998) Dislocations, grain size and planar faults in nanostructured copper determined by high resolution X-ray diffraction and a new procedure of

peak profile analysis. Acta Mater 46:3693–3699. https://doi.org/10.1016/S1359-6454(98)00001-9

[14] Ungár T, Dragomir I, Révész Á, Borbély A (1999) The contrast factors of dislocations in cubic crystals: the dislocation model of strain anisotropy in practice. J Appl Crystallogr 32:992–1002. https://doi.org/10.1107/S0021889899009334

[15] Shintani T, Murata Y (2011) Evaluation of the dislocation density and dislocation character in cold rolled Type 304 steel determined by profile analysis of X-ray diffraction. Acta Mater 59:4314–4322. https://doi.org/10.1016/j.actamat.2011.03.055

[16] Hielscher R, Schaeben H (2008) A novel pole figure inversion method: specification of the *MTEX* algorithm. J Appl Crystallogr 41:1024–1037. https://doi.org/10.1107/S0021889808030112

[17] Weibull W (1951) A Statistical Distribution Function of Wide Applicability. Journal of Applied Mechanics 293–297

[18] Kamaya M, Wilkinson AJ, Titchmarsh JM (2005) Measurement of plastic strain of polycrystalline material by electron backscatter diffraction. Nucl Eng Des 235:713–725. https://doi.org/10.1016/j.nucengdes.2004.11.006

[19] Brewer LN, Othon MA, Young LM, Angeliu TM (2006) Misorientation mapping for visualization of plastic deformation via electron back-scattered diffraction. Microsc Microanal 12:85–91. https://doi.org/10.1017/S1431927606060120

[20] Taylor GI (1934) The mechanism of plastic deformation of crystals. Part I. —Theoretical. Proc Royal Soc Lond Ser A Contain Papers Math Phys Character 145:362–387. https://doi.org/10.1098/rspa.1934.0106

[21] Pelleg J (2013) Mechanical Properties of Materials. Springer, Berlin

[22] Courtney TH (2005) Mechanical Behavior of Materials: Second Edition. Waveland Press

[23] Qin W, Li J, Liu Y et al (2019) Effects of grain size on tensile property and fracture morphology of 316L stainless steel. Mater Lett 254:116–119. https://doi.org/10.1016/j.matlet.2019.07.058

[24] Sylwestrowicz W, Hall EO (1951) The deformation and ageing of mild steel. Proc Phys Soc B 64:495–502. https://doi.org/10.1088/0370-1301/64/6/305

[25] Rodriguez P (1996) Sixty years of dislocations. Bull Mater Sci 19:857–872. https://doi.org/10.1007/BF02744623

[26] Davoudi KM, Vlassak JJ (2018) Dislocation evolution during plastic deformation: Equations vs. discrete dislocation dynamics study. Journal of Applied Physics 123:085302. https://doi.org/10.1063/1.5013213

[27] Pei C, Shi D, Yuan H, Li H (2019) Assessment of mechanical properties and fatigue performance of a selective laser melted nickel-base superalloy Inconel 718. Mater Sci Eng, A 759:278–287. https://doi.org/10.1016/j.msea.2019.05.007

[28] Withers PJ, Bhadeshia HKDH (2001) Residual stress. Part 1 – Measurement techniques. Mater Sci Technol 17:355–365. https://doi.org/10.1179/026708301101509980

[29] Withers PJ, Bhadeshia HKDH (2001) Residual stress. Part 2 – Nature and origins. Mater Sci Technol 17:366–375. https://doi.org/10.1179/026708301101510087

[30] Askeland DR, Fulay PP (2009) Essentials of materials science and engineering, 2nd ed. Cengage Learning, Australia; United States

[31] Huntington HB, Grone AR (1961) Current-induced marker motion in gold wires. J Phys Chem Solids 20:76–87. https://doi.org/10.1016/0022-3697(61)90138-X

[32] Conrad H (2000) Electroplasticity in metals and ceramics. Mater Sci Eng, A 287:276–287. https://doi.org/10.1016/S0921-5093(00)00786-3

[33] Xiang S, Zhang X (2019) Dislocation structure evolution under electroplastic effect. Mater Sci Eng, A 761:138026. https://doi.org/10.1016/j.msea.2019.138026

[34] Tang Y, Hosoi A, Iwase Y, Ju Y (2013) Effect of high-density electric current on the microstructure and fatigue crack initiation of stainless steel. Mater Trans 54:2085–2092. https://doi.org/10.2320/matertrans.M2013198

[35] Yuichi I (2014) The effect of high-density electric current on dislocation annihilation and fatigue crack initiation of metallic material. Master thesis, Nagoya University

[36] Moussa C, Bernacki M, Besnard R, Bozzolo N (2015) About quantitative EBSD analysis of deformation and recovery substructures in pure Tantalum. IOP Conf Ser: Mater Sci Eng 89:012038. https://doi.org/10.1088/1757-899X/89/1/012038

[37] Song H, Wang Z-J (2008) Microcrack healing and local recrystallization in pre-deformed sheet by high density electropulsing. Mater Sci Eng, A 490:1–6. https://doi.org/10.1016/j.msea.2007.12.037

[38] Song H, Wang Z, He X, Duan J (2017) Self-healing of damage inside metals triggered by electropulsing stimuli. Sci Rep 7:7097. https://doi.org/10.1038/s41598-017-06635-9

[39] Yang CL, Yang HJ, Zhang ZJ, Zhang ZF (2018) Recovery of tensile properties of twinning-induced plasticity steel via electropulsing induced void healing. Scripta Mater 147:88–92. https://doi.org/10.1016/j.scriptamat.2018.01.008

[40] Chen Z, Butcher C (2013) Introduction to Ductile Fracture Modelling. In: Chen Z, Butcher C (eds) Micromechanics Modelling of Ductile Fracture. Springer, Netherlands, Dordrecht, pp 1–24

[41] Lubarda VA, Schneider MS, Kalantar DH et al (2004) Void growth by dislocation emission. Acta Mater 52:1397–1408. https://doi.org/10.1016/j.actamat.2003.11.022